Investigation of the influence of additional magnets positions on four-magnet bi-stable piezoelectric energy harvester

Xinxin LI*, **Kexue HUANG**, **Zhilin LI**, **Jiangshu XIANG**, **Zhenfeng HUANG**, **Hanling MAO**, and **Yadong CAO**

College of Mechanical Engineering, Guangxi University, Nanning, China

Abstract. To enhance the harvesting performance of a bi-stable piezoelectric energy harvester (BEH), this work proposes a four-magnet BEH (FBEH). FBEH consists of a piezoelectric cantilever beam with a tip magnet, a fixed magnet and two movable magnets. The two movable magnets relative to the fixed magnet can move in both horizontal and vertical directions. A nonlinear distributed parameter model of FBEH is derived through the Hamilton principle. The effects of the excitation frequency and amplitude as well as the horizontal and vertical gap on the harvesting performance are mainly investigated by using the bifurcation diagram, phase diagram, Poincaré map and output power. Numerical simulations demonstrate that the proposed FBEH decreases the potential barrier and creates a higher than typical bi-stable one when subjected to lower excitation amplitudes and frequencies.

Key words: bi-stable; piezoelectric energy harvesting; nonlinear dynamic; potential energy.

1. INTRODUCTION

Energy harvesting, i.e. converting ambient energy into electric energy, has attracted extensive attention in the field of wireless sensor networks and MEMS. Among ambient energy sources, mechanical vibration energy is one of most potential and promising energy sources for its ubiquitous presence in the realistic environment. Harvesting electrical energy from ambient vibration energy provides an alternative to electrochemical batteries as a power source. Due to higher energy conversion efficiency and anti-electromagnetic interference, a piezoelectric vibration energy harvester (PEH) has proved to be the most attractive and emerging realization for this application. PEH have numerous advantages as not only do they reduce the maintenance costs required and eliminate the chemical hazards associated with regular batteries, but they also lead us towards a more sustainable world [1–8].

Initially, most of PEH was designed as a linear energy harvester (LEH) by means of adopting linear resonance theory [9, 10]. However, LEH can only perform efficiently in a narrow range near its natural frequency. To deal with this issue, different ways have been developed to broaden its bandwidth, including but not limited to active or passive frequency-tuning methods [11,12] and nonlinear methods that were monostable [13, 14], bi-stable [15–20] and multi-stable [21–25]. Among these methods, nonlinear methods capture much interest because of their abilities to expand bandwidth to lower frequencies. Bi-stable PEH (BEH) as the base of multi-stable

PEH, have many qualities worth studying. Yet the issue of entering and maintaining a high-energy orbit in its inter-well under lower excitation remains a challenging one.

To improve the harvesting performance of typical BEH (TBEH) at low-level excitation, researchers have put forward many modified methods. Wang *et al.* [26] designed a double BEH for enhancing harvesting efficiency over different excitation levels. Both simulations and experiments indicated that it can harvest more energy than TBEH. Wang *et al.* [27] utilized an elastic magnifier to amplify its base excitation. Through adjusting its mass and stiffness ratio, the presented BEH can provide sufficiently kinetic energy to overcome the potential barriers over broader bandwidth and lower excitation. Zhou *et al.* [28] presented a nonlinear flexible BEH, and its simulation results demonstrated that the proposed harvester has a smaller threshold for snap-through and thus generates larger output power. Li *et al.* [29] designed a novel spring-connected BEH, and numerical simulations showed that its potential barrier was reduced and snap-through triggered easily under lower excitation.

To further enhance the harvesting performance of TBEH under lower excitations, bi-stability can also be extended to multistable energy harvesters through additional magnets to increase the number of equilibrium or stable states. Multi-stable energy harvesters reduce the potential barriers and render the snapthrough motion easier. Zhou *et al.* [30, 31] proposed tri-stable and penta-stable energy harvesters, respectively, and their numerical and experimental results verified the harvesting performance improved under lower excitation. Huang *et al.* [32] focused on the theoretical analysis of a multi-stable energy harvester with high-order stiffness terms to reveal their dynamic response mechanism and enhance its harvesting performance.

Lan *et al.* [33] proposed an improved BEH, and their simulation results demonstrated that it also can produce high voltage output at lower excitation. However, the additional magnets of the above harvesters were aligned with the fixed magnet of TBEH and the influence of the two magnets' positions is not yet investigated.

Based on TBEH and inspired by the above-mentioned studies, this work proposed a four-magnet BEH (FBEH). Two additional magnets are positioned around the middle fixed magnet to reduce the potential barrier, aiming to enhance harvesting performance at lower excitations. Through the adjustment of the position parameters, the impact of additional magnets' positions on harvesting performance is studied. The simulation results demonstrated that FBEH can improve harvesting performance by selecting appropriate parameters when in lower excitations.

The rest of this paper is organized as follows. In Section 2, the configuration of FBEH is illustrated and then the governing equations of motion are derived based on the Hamilton principle. In Section 3, the effects of additional magnets' positions on potential barriers are demonstrated. In Section 4, the effects of the excitation amplitude and frequency on the harvesting performance for FBEH with different parameters are studied, mainly through a bifurcation diagram, phase diagram, Poincaré map and output power. And the discussions are conducted in Section 5. The conclusions are drawn at last.

2. FBEH CONFIGURATION AND MATHEMATICAL MODELING

Commonly, TBEH consists of a piezoelectric cantilever beam, a tip magnet (magnet A) and a fixed magnet (magnet B). The tip and fixed magnets with the same polarity facing each other are separated by distance d as measured from their centers. Two additional movable magnets (magnets C and D) are added to TBEH to form FBEH. The gaps between the two additional magnets and the fixed magnet in the vertical and horizontal direction are s and c, respectively. The proposed FBEH configuration is shown as Fig. 1(a). For further experimental research, the experimental setup is presented in Fig. 1(b). The FBEH is excited by an electromagnetic shaker, driven by a power amplifier. A function generator provides the harmonic signal as the input of the amplifier. An accelerator is placed on the base to measure the excitation, and the voltage output of the piezoelectric element is acquired by an oscilloscope. The adjustment configurations of the positions of magnets C and D are also presented in Fig. 1(c). On the one hand, magnet C is clamped on the edge of the upper one of the three movable clampers. The clamper is placed in the hollow block and its position can be changed to regulate magnet C's horizontal distance s. On the other hand, the hollow movable block can be adjusted along with the aluminum pillar in the vertical direction to change distance c of magnet C. Distances s and c of magnet D can be adjusted in a similar manner. Referring to the scales on the blocks and the aluminum pillar, the positions of magnets C and D can be regulated according to the requirements of different systems.
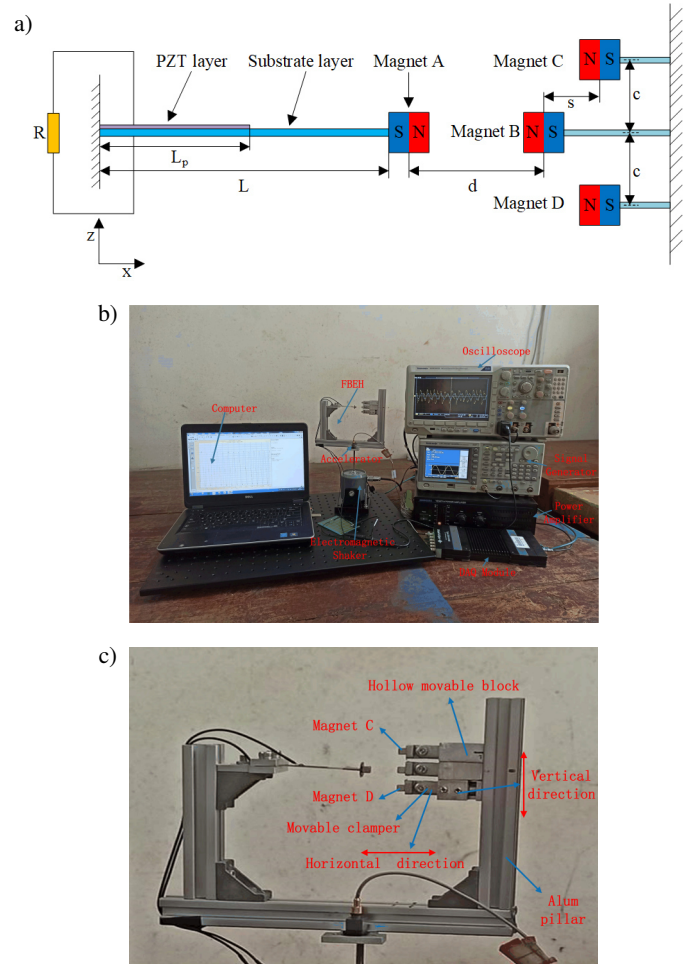

Fig. 1. Proposed FBEH configuration: (a) schematic diagram of FBEH; (b) experimental setup for further research; (c) configuration of magnet C and D for position adjustment

To investigate the FBEH theoretically, Lagrange function [34] can be applied and then written as:

$$l(x,t) = T_S + T_P + T_M + W_P - U_S - U_P - U_{mB} - U_{mC} - U_{mD}, \quad (1)$$

where T_S, T_P and T_M are the kinetic energy of the substrate, piezoelectric layer and tip magnet, respectively; W_P is the electric energy produced by the piezoelectric layer; U_S and U_P denote the elastic potential energy of the substrate and piezoelectric layer, separately; and U_{mB}, U_{mB} and U_{mD} represent magnetic potential energy generated by magnets B, C and D on magnet A, respectively.

As for the proposed FBEH, the kinetic energy within each layer is distributed along length L of the cantilever beam for the substrate layer as:

$$T_S = \frac{1}{2} \int_{V_S} \rho_S \left(\frac{\partial(u(x,t))}{\partial t} \right)^2 dV_S$$

$$= \frac{1}{2} \rho_S A_S \int_0^L \left(\frac{\partial(w(x,t))}{\partial t} + \dot{z}(t) \right)^2 dx, \quad (2)$$

2

Bull. Pol. Acad. Sci. Tech. Sci., vol. 70, no. 1, p. e140151, 2022

and for the piezoelectric layer as:

$$
T_P = \frac{1}{2} \int_{V_P} \rho_P \left(\frac{\partial (u(x,t))}{\partial t} \right)^2 dV_P
$$

$$
= \frac{1}{2} \rho_P A_P \int_0^L \left(\frac{\partial (w(x,t))}{\partial t} + \dot{z}(t) \right)^2 H(x) \, dx, \qquad (3)
$$

where the overdot denotes the derivative with respect to time t; ρ_S and ρ_P are the substrate and piezoelectric material density, separately; V_S and V_P represent the volume of the substrate and piezoelectric layer, respectively; A_S and A_P are the cross-sectional areas of the substrate and piezoelectric layer, separately; L and L_P denote the substrate and piezoelectric layer length, respectively; $\dot{z}(t)$ is base vibration speed; $u(x,t)$ is the absolute deflection; $w(x,t)$ is the transverse deflection; and $H(x)$ is the Heaviside step function given by:

$$
H(x) = H(x) - H(x - L_P). \qquad (4)
$$

The end mass, magnet A, additionally has the kinetic energy of similar form:

$$
T_M = \frac{1}{2} M_t \left(\left[\frac{\partial (w(x,t))}{\partial t} \right]_{x=L} + \dot{z}(t) \right)^2 \qquad (5)
$$

in which M_t is the mass of magnet A, and rotational inertia can be negligible.

After deformation of the piezoelectric layer is generated, the electric energy created by the piezoelectric effect can be evaluated by the following:

$$
W_P = \frac{1}{2} \int_{V_P} E_3 D_3 \, dV_P
$$

$$
= \frac{1}{2} \int_{V_P} E_3 \left(e_{31} S_1 + \varepsilon_{33}^S E_3 \right) dV_P
$$

$$
= \frac{1}{4} e_{31} v(t)(h_s + h_p) b \left. \frac{\partial (w(x,t))}{\partial x} \right|_{x=L_P}
$$

$$
+ \frac{1}{2h_p} \varepsilon_{33}^S L_P b v(t)^2, \qquad (6)
$$

where E_3 and D_3 represent the electric field strength and electric displacement, respectively; h_S and h_P are the substrate and piezoelectric layer thicknesses, respectively; b denotes the cantilever beam width; ε_{33}^S is the permittivity constant of the piezoelectric layer; e_{31} is the electromechanical coupling coefficient; S_1 refers to the mechanical strain. $v(t)$ denotes the output voltage, and:

$$
v(t) = R \dot{q}(t), \qquad (7)
$$

where R denotes the load resistance and $\dot{q}(t)$ is the electric charge of the piezoelectric layer. The elastic potential energy of

the substrate and piezoelectric layer are separately expressed as:

$$
U_S = \frac{1}{2} \int_{V_S} T_S S_S \, dV_S = \frac{1}{2} E_S I_S \int_0^L \left(\frac{\partial^2 (w(x,t))}{\partial x^2} \right)^2 dx, \qquad (8)
$$

$$
U_P = \frac{1}{2} \int_{V_P} T_1 S_1 \, dV_P = \frac{1}{2} E_P I_P \int_0^{L_p} \left(\frac{\partial^2 (w(x,t))}{\partial x^2} \right)^2 H(x) \, dx
$$

$$
- \frac{1}{4} e_{31} v(t)(h_s + h_p) b \left. \frac{\partial (w(x,t))}{\partial x} \right|_{x=L_p}, \qquad (9)
$$

in which T_S and S_S refer to the axial stress and strain of the substrate layer; T_1 is the axial stress of the piezoelectric layer; E_S and E_P are Young's modulus of the substrate and piezoelectric layer, respectively; and I_S and I_P represent area moment of inertia for the substrate and piezoelectric layer, separately.

The magnets geometric relationship is shown in Fig. 2. Based upon magnetic dipole theory, magnetic potential energy generated by magnet A on magnets B, C or D can be formulated, respectively, as [35]:

$$
U_{mB} = \frac{\mu_0}{4\pi} \left[\frac{m_A}{\|r_{AB}\|_2^3} - \frac{(m_A \cdot r_{AB}) \cdot 3 r_{AB}}{\|r_{AB}\|_2^5} \right] m_B, \qquad (10)
$$

$$
U_{mC} = \frac{\mu_0}{4\pi} \left[\frac{m_A}{\|r_{AC}\|_2^3} - \frac{(m_A \cdot r_{AC}) \cdot 3 r_{AC}}{\|r_{AC}\|_2^5} \right] m_C, \qquad (11)
$$

$$
U_{mD} = \frac{\mu_0}{4\pi} \left[\frac{m_A}{\|r_{AD}\|_2^3} - \frac{(m_A \cdot r_{AD}) \cdot 3 r_{AD}}{\|r_{AD}\|_2^2} \right] m_D, \qquad (12)
$$

here $\| \ \|_2$ is the Euclidean norm; μ_0 represents the vacuum permeability of free space; r_{AB}, r_{AC} and r_{AD} are the vectors from the center of magnet A to the center of magnets B, C and D, respectively; and m_A, m_B, m_C and m_D denote the magnetic moment vectors of magnets A, B, C and D, separately.
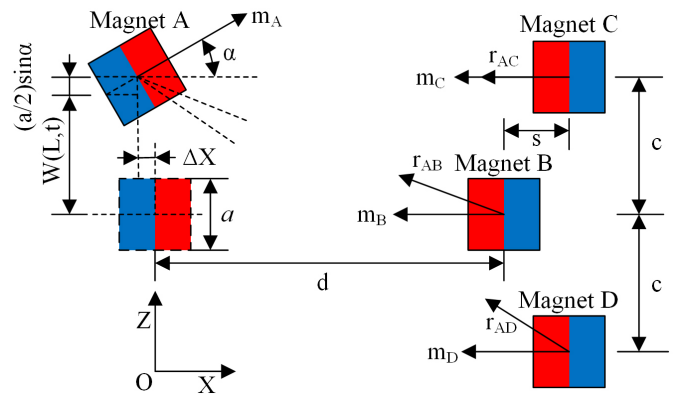

Fig. 2. Schematic diagram of magnets geometric relationship

The magnetic moment vectors can be calculated as:

$$
m_A = [M_A V_A \cos\alpha \quad M_A V_A \sin\alpha], \quad m_B = [-M_B V_B \quad 0], \qquad (13)
$$

$$
m_C = [-M_C V_C \quad 0], \qquad\qquad m_D = [-M_D V_D \quad 0], \qquad (14)
$$

Bull. Pol. Acad. Sci. Tech. Sci., vol. 70, no. 1, p. e140151, 2022

3

where M_A, M_B, M_C and M_D refer to the magnetization vector of magnets A, B, C and D, respectively; V_A, V_B, V_C and V_D represent the volume of the magnet; and α is the rotational slope of the tip magnet (magnet A) and satisfies the following relation:

$$\alpha = \arctan(\dot{w}(L,t)). \tag{15}$$

Neglecting the translation of the magnet, the direction vectors r_{AB}, r_{AC}, r_{AD} can be separately expressed as:

$$r_{AB} = [d - w(L,t)], \tag{16}$$

$$r_{AC} = [d + sc - w(L,t)], \tag{17}$$

$$r_{AD} = [d + sc + w(L,t)]. \tag{18}$$

After inserting equations (13) to (18) into equations (10) to (12) and simplifying them, the magnetic potential energy produced by magnets B, C or D on magnet A can be respectively rewritten as:

$$U_{mB} = \left(\mu_0 M_A V_A M_B V_B(-w(L,t)^2 + 2d^2 - 3dw(L,t)\dot{w}(L,t))\right) \Big/ \left(4\pi\sqrt{((\dot{w}(L,t))^2 + 1)}\left(w(L,t)^2 + d^2\right)^{5/2}\right), \tag{19}$$

$$U_{mC} = \left(\mu_0 M_A V_A M_C V_C(-(c - w(L,t))^2 + 2(d+s)^2 \right. \\ \left. - 3(d+s)(c - w(L,t))\dot{w}(L,t))\right) \Big/ \\ \left(4\pi\sqrt{((\dot{w}(L,t))^2 + 1)}((c - w(L,t))^2 + (d+s)^2)^{5/2}\right), \tag{20}$$

$$U_{mD} = \left(\mu_0 M_A V_A M_D V_D(-(c + w(L,t))^2 + 2(d+s)^2 \right. \\ \left. - 3(d+s)(c + w(L,t))\dot{w}(L,t))\right) \Big/ \\ \left(4\pi\sqrt{((\dot{w}(L,t))^2 + 1)}((c + w(L,t))^2 + (d+s)^2)^{5/2}\right). \tag{21}$$

That is, assuming the piezoelectric beam conformity with Euler-Bernoulli beam theory. By applying the first mode approximation, $w(x,t)$ can be expressed in terms of the first mode of shape function and temporal displacement, respectively:

$$w(x,t) = \emptyset(x)r(t), \tag{22}$$

where the first mode shape function $\emptyset(x)$ can be written as:

$$\emptyset(x) = 1 - \cos\frac{\pi x}{2l}. \tag{23}$$

Substituting equations (2) to (3), (5) to (6), (8) to (9), and (19) to (21) into equation (1), the Lagrange function of FBEH can be evaluated as:

$$l(x,t) = \frac{1}{2}\rho_S A_S \int_0^L (\emptyset(x)\dot{r}(t) + \dot{z}(t))^2 \, \mathrm{d}x$$

$$+ \frac{1}{2}\rho_P A_P \int_0^L (\emptyset(x)\dot{r}(t) + \dot{z}(t))^2 H(x) \, \mathrm{d}x$$

$$+ \frac{1}{2}M_t(\emptyset(L)\dot{r}(t) + \dot{z}(t))^2$$

$$+ \frac{1}{2}e_{31}v(t)(h_s + h_p)b\dot{\emptyset}(L_P)r(t) + \frac{1}{2h_p}\varepsilon_{33}^S L_P bv(t)^2$$

$$- \frac{1}{2}E_S I_S \int_0^L (\ddot{\emptyset}(x)^2 r(t)^2) \, \mathrm{d}x$$

$$- \frac{1}{2}E_P I_P \int_0^L (\ddot{\emptyset}(x)^2 r(t)^2) H(x) \, \mathrm{d}x - U_m(r(t)). \tag{24}$$

According to the Euler–Lagrange equation and considering viscous damping and output charge, the electromechanical coupling dynamic governing equations can be derived as follows:

$$\begin{cases} M_0\ddot{r} + C_0\dot{r} + K_0 r + \dfrac{\partial U_m}{\partial r} - \theta v = -\daleth\ddot{z}(t), \\ \theta\dot{r} + C_p\dot{v} = -\dfrac{v}{R}, \end{cases} \tag{25}$$

where M_0, K_0, θ, $\daleth$ and C_p can be given by:

$$M_0 = \rho_S A_S \int_0^L (\emptyset(x))^2 \, \mathrm{d}x$$

$$+ \rho_P A_P \int_0^L (\emptyset(x))^2 H(x) \, \mathrm{d}x + M_t \emptyset(L)^2, \tag{26}$$

$$K_0 = \frac{1}{2}E_S I_S \int_0^L \ddot{\emptyset}(x) \, \mathrm{d}x + \frac{1}{2}E_P I_P \int_0^L \ddot{\emptyset}(x) H(x) \, \mathrm{d}x, \tag{27}$$

$$\theta = \frac{1}{2}e_{31}v(h_s + h_p)b\dot{\emptyset}(L_P), \tag{28}$$

$$\daleth = \rho_S A_S \int_0^L \emptyset(x) \, \mathrm{d}x + \rho_P A_P \int_0^L \emptyset(x)H(x) \, \mathrm{d}x + M_t\emptyset(L), \tag{29}$$

$$C_p = \frac{1}{h_p}\varepsilon_{33}^S L_P b, \tag{30}$$

and $\partial U_m/\partial r$ represents the partial derivative of magnetic potential energy U_m with respect to temporal displacement $r(t)$, while C_0 is the piezoelectric cantilever damping.

Equation set (25) can be further nondimensionalized through introducing the following dimensionless quantities:

$$r(t) = lX(\tau), \qquad \tau = \omega_0 t,$$

$$z(t) = \frac{lM_0}{\daleth}Z(\tau), \quad v(t) = \frac{K_0 l}{\theta}V(\tau), \tag{31}$$

4

Bull. Pol. Acad. Sci. Tech. Sci., vol. 70, no. 1, p. e140151, 2022

in which l is a length scale and $\omega_0 = \sqrt{K_0/M_0}$ represents the natural frequency. This gains the following non-dimensional equations:

$$\begin{cases} \ddot{X} + \xi\dot{X} + X + \partial U_m/\partial X - V = -\ddot{Z}, \\ \kappa^2\dot{X} + \dot{V} + \vartheta V = 0, \end{cases} \tag{32}$$

where:

$$\xi = \frac{C_0}{M_0\omega_0}, \quad \kappa^2 = \frac{\theta^2}{C_pK_0}, \quad \vartheta = \frac{1}{C_pR\omega_0} \tag{33}$$

and U_m is the total magnetic potential energy for FBEH, i.e. $U_m = U_{mB} + U_{mC} + U_{mD}$.

For the proposed FBEH, we mainly investigate the harvesting performance under harmonic excitation. Hence, we assume that the dimensionless harmonic base excitation can be represented by:

$$\ddot{Z} = A\cos(\omega\tau), \quad \omega = \frac{\Omega}{\omega_0}, \tag{34}$$

where ω and A denote the dimensionless excitation frequency and amplitude, respectively. Hence the form of state-space for equation set (32) can be expressed as:

$$\begin{Bmatrix} \dot{x}_1 \\ \dot{x}_2 \\ \dot{x}_3 \end{Bmatrix} = \begin{Bmatrix} x_2 \\ -\xi x_2 - x_1 - \partial U_m/\partial x_1 + x_3 - A\cos(\omega\tau) \\ -\kappa^2 x_2 - \vartheta x_3 \end{Bmatrix}, \tag{35}$$

in which the state variables are $x_1 = X$, $x_2 = \dot{X}$ and $x_3 = V$.

3. POTENTIAL ENERGY ANALYSIS

To illustrate the variation of potential energy for FBEH after magnets C and D are introduced, the expression of potential energy of FBEH can be written as:

$$U(X) = U_k(X) + U_m(X) = \frac{1}{2}K_0l^2X^2 + U_m(X). \tag{36}$$

The potential energy of a FBEH system ($s = 2$, $c = 11$) for FBEH and TBEH can be plotted as shown in Fig. 3 via equation (36) with the given parameter values. It can be seen from Fig. 3
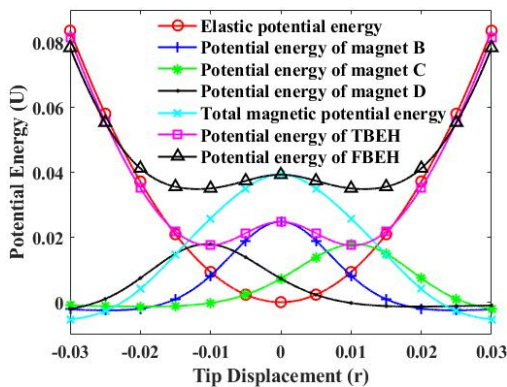
Fig. 3. Potential energy for a FBEH system

that the magnetic potential energy generated by two additional magnets can obviously widen the potential well of TBEH.

To study the relationship between the potential energy and the horizontal or vertical gap s or c, magnet material in FBEH is assumed to be homogenous and consistent, and its volume and gap d between magnets A and B are constant. The potential energies of magnets B, C, and D acting on magnet A are shown in Fig. 4(b) and Fig. 4(d) for the different vertical gap c between magnets C or D and magnet B ($c_1 < c_2 < c_3$). Similarly, the potential energy of only magnet C or D exerting to magnet A are depicted in Fig. 4(a) and Fig. 4(c) for the different horizontal gap s between magnets C or D and magnet B ($s_1 < s_2 < s_3$). From Fig. 4(b) and Fig. 4(d), it has an identical varying trend and their shapes are centrally symmetric owing to magnets C and D being deployed symmetrically.
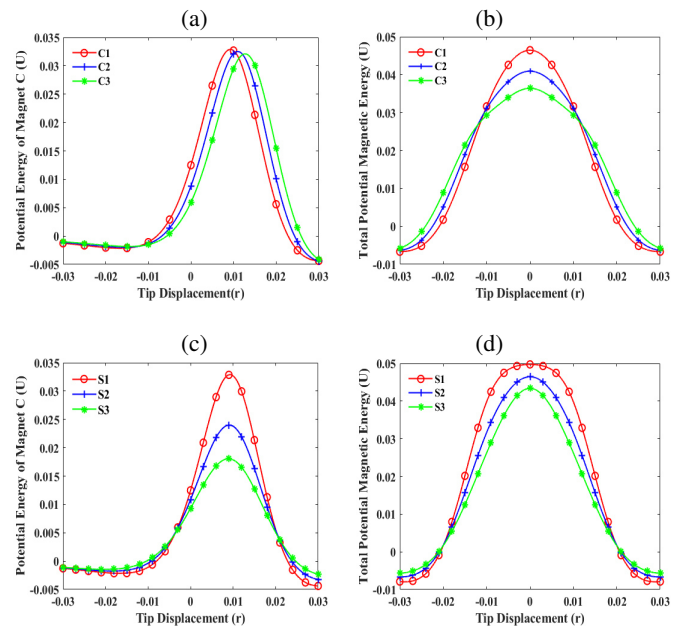
Fig. 4. Potential energy: (a) and (c) only magnet C acting on magnet A for different vertical gap c; (b) and (d) magnets B, C, or D acting on magnet A for different horizontal gap s

It is shown in Fig. 4(a) and 4(c) that as the vertical gap c increases, the potential energy of only magnet C acting on magnet A shifts towards the right, and the total potential energy of magnets B, C and D imposing to magnet A shrinks downwards. From Fig. 4(b) and 4(d) it is known that with the decreasing of horizontal gap s, the potential energy of only magnet C applied to magnet A shows an upward trend, and the total potential energy of magnets B, C and D exerting to magnet A expands to both sides.

4. NUMERICAL SIMULATIONS

In this section, numerical simulations were carried out to examine the nonlinear behaviors and harvesting performances of FBEH with different shapes of potential energy and TBEH for different excitation levels. The parameters and values of FBEH and TBEH are listed in Table 1. In order to be compared with

Table 1
Parameters and values of FBEH

Symbols	Parameters (unit)	values
L	Length of substrate layer (mm)	45
Lp	Length of piezoelectric layer (mm)	25
hs	Thickness of substrate layer (mm)	0.2
hp	Thickness of piezoelectric layer (mm)	0.25
ρ_s	Density of substrate layer (kg/m^3)	7900
ρ_p	Density of piezoelectric layer (kg/m^3)	7600
E_S	Young's modulus of substrate layer (GPa)	113
E_p	Young's modulus of piezoelectric layer (GPa)	62
b	Width of substrate layer (mm)	10
e_{31}	Piezoelectric coupling coefficient (C/m^2)	–21.08
ε_{33}^S	Permittivity constant (nF/m)	44.27
M_{mi}	Mass of magnet ($i = A, B, C, D$) (g)	6.4
V_i	Volume of magnet ($i = A, B, C, D$) (mm^3)	1000
M_i	Residual flux density ($i = A, B, C, D$) (T)	1.25
R	Load resistance (kΩ)	100

each other, gap d between magnets A and B was set as 20 mm for both FBEH and TBEH here. Also, the horizontal gap s between magnet C or D and magnet B is set as –2 mm, 0 mm, or 2 mm, and vertical gap c between them is set as 11 mm, 13 mm, or 15 mm, respectively. As a result, 9 systems for FBEH are obtained. For convenience, these 9 systems are numbered from 1 to 9, as shown in Table 2, and divided into three groups according to horizontal gap s. Each group has three different vertical gaps c. System 0 represents TBEH.

Table 2
Numbered systems of FBEH

s value	$c = 11$ mm	$c = 13$ mm	$c = 15$ mm
–2 mm	1	2	3
0 mm	4	5	6
2 mm	7	8	9

The effect of potential energy on output performance is analyzed through output power, phase diagram, Poincaré maps and bifurcation diagrams. In these simulations, the excitation frequency range is set as $\omega = [0.1, 1.2]$, and the excitation amplitude range is set as $A = [0.02, 0.24]$. To reveal harvesting performance of FBEH in lower excitations, $\omega = 0.2$ and $A = 0.04$ are taken as representative of lower excitations to respectively investigate effects of excitation amplitude and frequency on harvesting performance.

4.1. Harvesting performance for *s* = –2 mm
Group 1 contains systems 1 to 3 listed in Table 2. The potential energy of group 1 systems as compared to TBEH is shown in Fig. 5. Two potential barriers and three potential wells presenting a tri-stable characteristic are observed in Fig. 5.
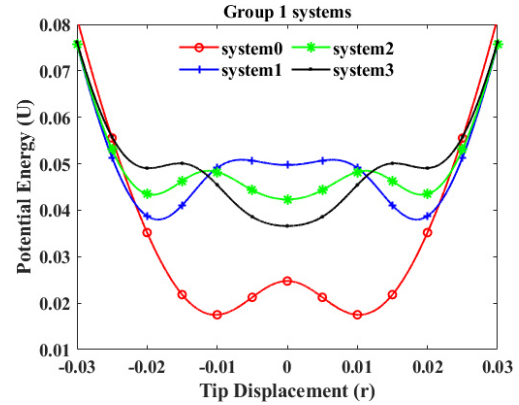

Fig. 5. Potential energy of group 1 systems

4.1.1. Effects of excitation amplitude on harvesting performance
Under excitation frequency ω of 0.2, an excitation amplitude ranging from 0.02 to 0.24 is adopted as a control parameter to examine the dynamic response of group 1 systems. The output power, phase diagram, Poincaré maps and bifurcation diagrams of these systems are shown as Fig. 6 and Fig. 7, respectively.
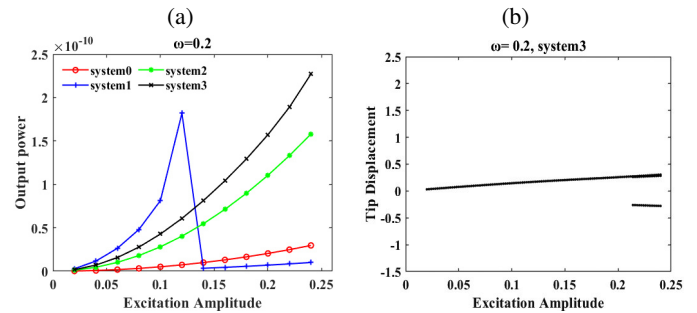

Fig. 6. Output power of group 1 systems at $\omega = 0.2$ for (a); bifurcation diagram of system 3 at $A = 0.12$ for (b)

From Fig. 6(a), it is obvious that the output power of system 1 increases firstly with increasing of excitation amplitude, but decreases dramatically when it comes to a certain amplitude level of $A = 0.12$ and performs even more poorly than system 0 once such threshold value is exceeded. In contrast, systems 2 and 3 increase all the time along the whole excitation amplitude range. The phase diagrams and Poincaré maps of systems 1 to 3 as excitation amplitude $A = 0.12$ are shown in Fig. 7. Compared with the equilibrium of the potential energy in Fig. 5, it can be found clearly that system 1 oscillates within the middle of the potential well, with smaller movement range of [–0.6, 0.6]. Because the middle potential well of system 1 is smaller than the other systems, it can cross the potential barrier and enter in the left or right-side of the potential well. And because of the deeper potential barriers in side potential wells, it results in a smaller intra-well orbit and output power reduction under the condition of the larger excitation level ranging from 0.14 to 0.24, as shown in Fig. 6(a). In contrast, systems 2 and 3 decrease the displacement range to [–0.4, 0.4] and [–0.5, 0.5], respectively, and generate less power output than system 1 at this

6

Bull. Pol. Acad. Sci. Tech. Sci., vol. 70, no. 1, p. e140151, 2022
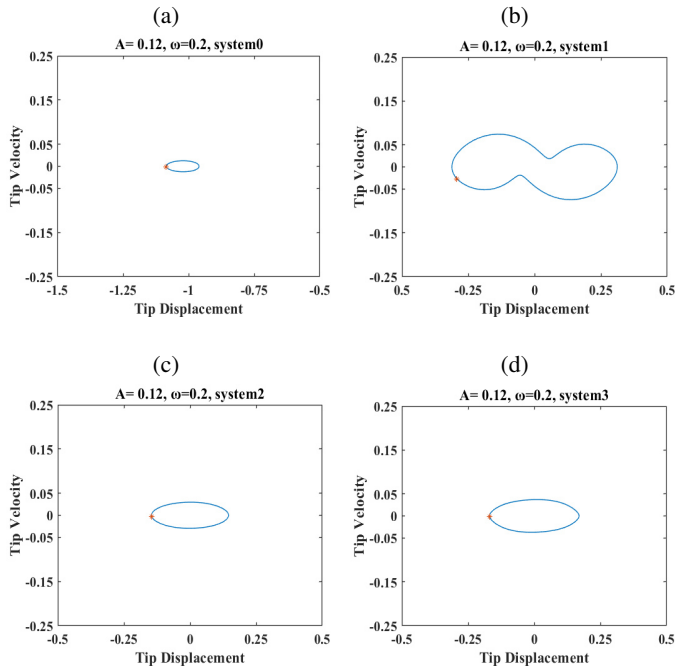
Fig. 7. Phase diagram (blue lines) and Poincaré map (red points) at $\omega = 0.2$ and $A = 0.12$ for (a) system 0; (b) system 1; (c) system 2; (d) system 3

moment. However, systems 2 and 3 present similar characteristics. And a larger excitation amplitude is required to improve their output power again. The bifurcation diagram of system 3 within the excitation amplitude range is shown in Fig. 6(b). A single periodic and then double periodic oscillation are indicated.

4.1.2. Effects of excitation frequency on harvesting performance

Under excitation amplitude $A = 0.04$, excitation frequency ranging from 0.1 to 1.2 is adopted as a control parameter to examine the dynamic response of group 1 systems.

The output power of systems 1 to 3 is shown in Fig. 8(a). It is obvious that system 1 present better harvesting performance than systems 2 and 3 when excitation frequency ranges between 0.6 and 0.8. It is especially greater than for system 0. For excitation frequency $\omega = 0.7$, the phase diagram and Poincaré map of systems 1 to 3 are depicted in Fig. 9. It is implied that sys-

tem 1 exhibits larger intra-well periodical orbits than systems 2 and 3 in the middle potential well of a tri-stable harvester, leading to significant improvement of output power. The bifurcation diagram of system 3 within the excitation frequency range of [0.1, 1.2] is shown in Fig. 8(b). It can be seen from that with the increase of excitation frequency, system 3 goes from the middle potential well intra-well movement to outer potential well intra-well motion, and back to the middle potential well intra-well movement, resulting in the output power increasing and then decreasing dramatically and later improving gradually.
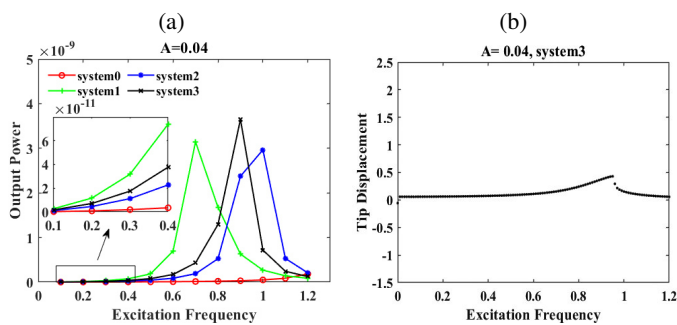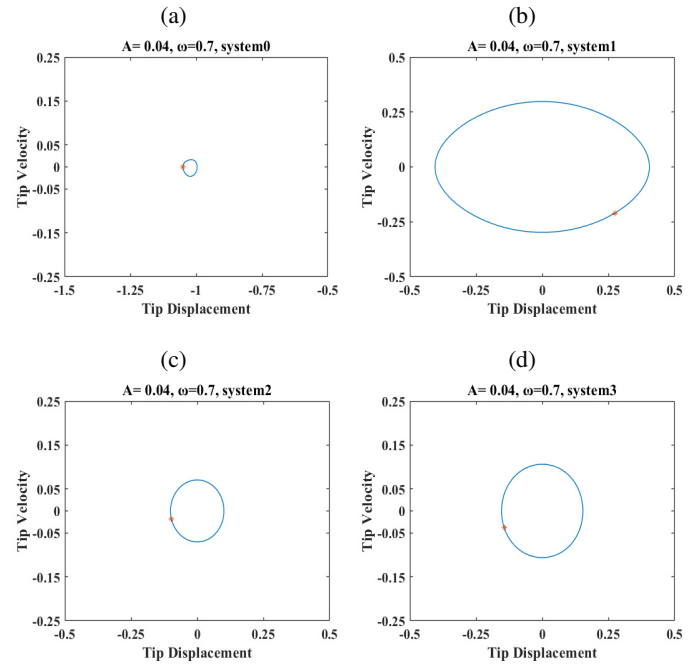

Fig. 9. Phase diagram (blue lines) and Poincaré map (red points) at $\omega = 0.7$ and $A = 0.04$ for (a) system 0; (b) system 1; (c) system 2; (d) system 3

4.2. Harvesting performance for s = 0 mm

Group 3 includes systems 7 to 9 listed in Table 2. The potential energy of group 2 systems is shown in Fig. 10. In Fig. 10, the potential barrier depth gradually decreases with the increasing of vertical gap c.
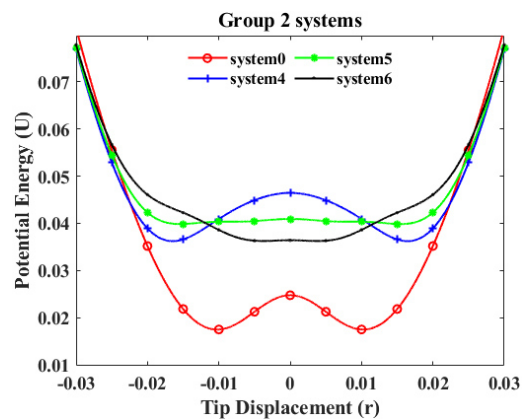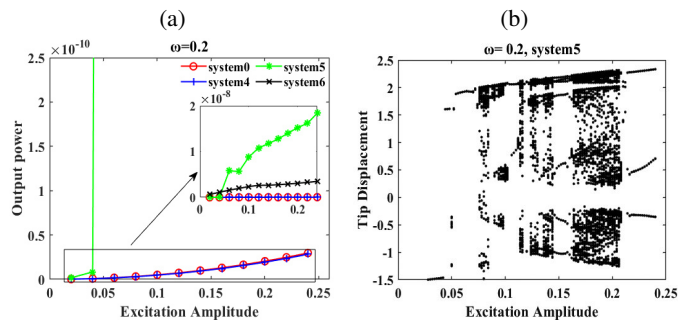

Fig. 10. Potential energy of group 2 systems

Fig. 8. Output power of group 1 systems at $A = 0.04$ for (a) and bifurcation diagram of system 3 at $A = 0.04$ for (b)

Bull. Pol. Acad. Sci. Tech. Sci., vol. 70, no. 1, p. e140151, 2022

7

4.2.1. Effects of excitation amplitude on harvesting performance

Excitation frequency as is set as $\omega = 0.2$ and the excitation amplitude ranges from 0.02 to 0.24. As a result, output power of systems 4 to 6 under different excitation amplitudes is as shown in Fig. 11(a). The shallower potential barriers of systems 5 to 6 facilitate entry into chaotic or inter-well orbits and harvest more energy at low excitation levels. In contrast, system 4 with potential barriers deeper than even those for system 0 becomes entrapped in the low-energy orbits of one of the two potential wells, leading to poor output power.

Fig. 11. Output power of group 1 systems at $A = 0.04$ for (a) and bifurcation diagram of system 3 at $A = 0.04$ for (b)

The phase diagram, Poincaré map and voltage response of systems 4 and 6 are shown in Fig. 12. It is known from Fig. 12 that when the excitation amplitude $A = 0.08$, system 5 experiences a higher vibration displacement amplitude and higher output voltage under its chaotic state, while system 6 is in its

left potential well with intra-well periodical movement. Due to a lower potential barrier, it is easier for system 5 than for systems 4 and 6 to realize the chaotic or inter-well motion and as a result, high harvesting performance. From Fig. 12 it is obvious that an abundance of chaos can effectively improve energy harvesting efficiency under a low excitation amplitude. The bifurcation diagram of system 5 at excitation frequency $\omega = 0.2$ is shown in Fig. 11(b). In Fig. 11(b), the excitation amplitude range occurring as a result of chaotic motion occupies the largest section of the whole excitation amplitude range.

4.2.2. Effects of excitation frequency on harvesting performance

Excitation amplitude is set as $A = 0.04$, and the excitation frequency ranging from 0.1 to 1.2 is adopted to examine the dynamic response of group 3 systems.

The output powers of systems 4 to 6 are shown as Fig. 13(a). It is manifested that system 6 can tremendously improve its harvesting performance at lower excitation frequencies, in contrast to system 0. The phase diagrams and Poincaré maps of systems 4 to 6 are shown in Fig. 14. It is shown in Fig. 14 that when excitation frequency was $\omega = 0.4$, system 6 came into high-energy inter-well orbits and obtained maximum output power, which means higher harvesting efficiency for low excitation frequency. The bifurcation diagram of system 6 is shown in Fig. 13(b). In Fig. 13(b), system 6 presents the intra-well motion, chaotic motion, bi-stable periodic motion and multiple periodic motion. Due to the rich nonlinear characteristics of that system, its bandwidth is extended, and output performance under low excitation frequency environment is greatly improved.
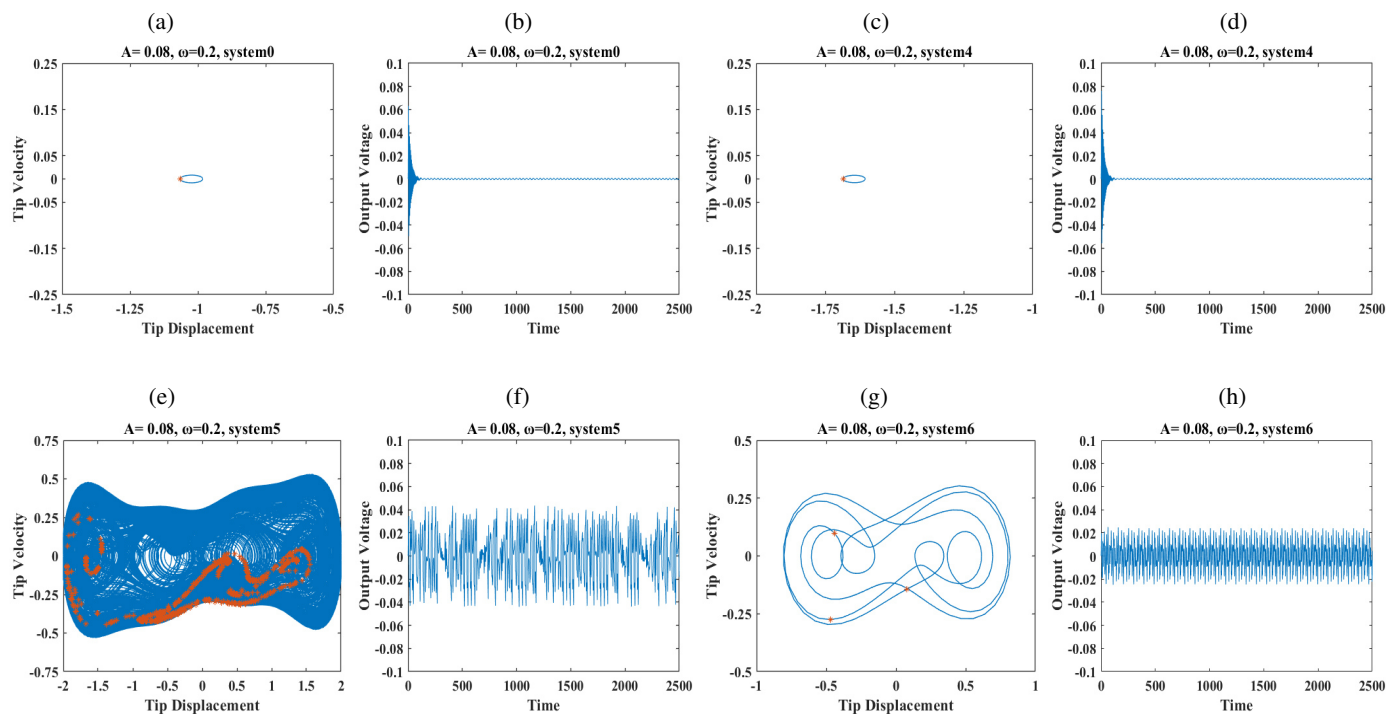

Fig. 12. Phase diagram (blue lines), Poincaré map (red points) and voltage response at $\omega = 0.2$ and $A = 0.08$ for (a) and (b) system 0; (c) and (d) system 4; (e) and (f) system 5; (g) and (h) system 6

8

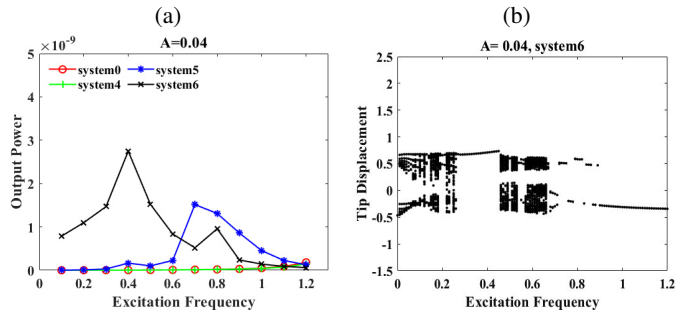*Bull. Pol. Acad. Sci. Tech. Sci.*, vol. 70, no. 1, e140151, 2022

Fig. 13. Output power of group 3 systems at $A = 0.2$ for (a) and bifurcation diagram of system 6 at $A = 0.2$ for (b)
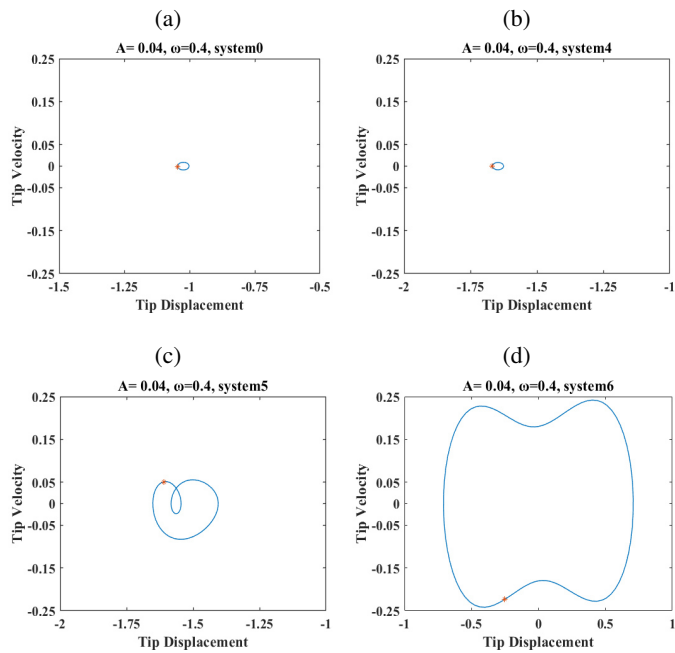

Fig. 14. Phase diagram (blue lines) and Poincaré map (red points) at $\omega = 0.7$ and $A = 0.04$ for (a) system 0; (b) system 1; (c) system 2; (d) system 3

4.3. Harvesting performance for *s* = 2 mm

Group 3 includes systems 7 to 9 listed in Table 2. The potential energy of group 3 systems is shown in Fig. 15. The potential energy of this group has bi-stable characteristics.
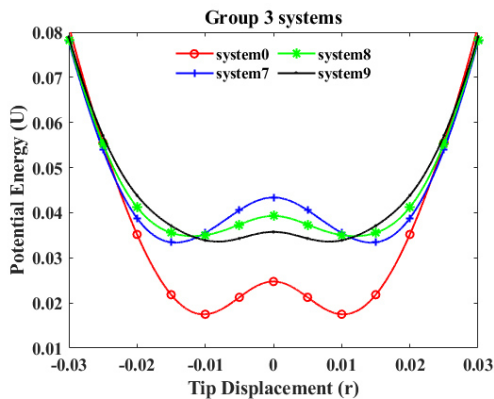

Fig. 15. Potential energy of group 3 systems

4.3.1. Effects of excitation amplitude on harvesting performance

Excitation frequency $\omega = 0.2$ and the range of excitation amplitude $A = [0.02, 0.24]$ is adopted to examine the dynamic response of group 3 systems. The output power of systems 7 to 9 is shown in Fig. 16(a).
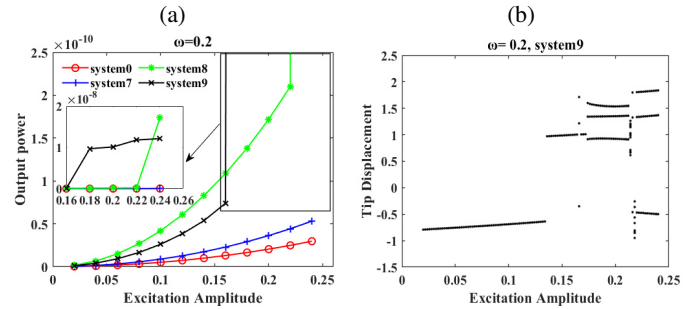

Fig. 16. Output power of group 3 systems at $\omega = 0.2$ for (a) and bifurcation diagram of system 9 at $\omega = 0.2$ for (b)

In Fig. 16(a), system 9 has better output power within a higher excitation amplitude range [0.18, 0.24], while system 8 has an ideal output power within a higher and narrower excitation amplitude range [0.22, 0.24]. Because system 7 has a potential energy shape and well-depth similar to those of system 0, there is almost no output power in the entire excitation amplitude range. For excitation amplitude $A = 0.18$, the phase diagram, Poincaré map and voltage response of systems 7 to 9 are shown in Fig. 17. It can be seen from Fig. 17 that both systems 7 and 8 oscillate in low energy intra-well orbits with vibration deflection of [−1.6, −1.2] and [−1.4, −0.8], respectively. However, system 9 can conduct chaotic, large amplitude periodic or their
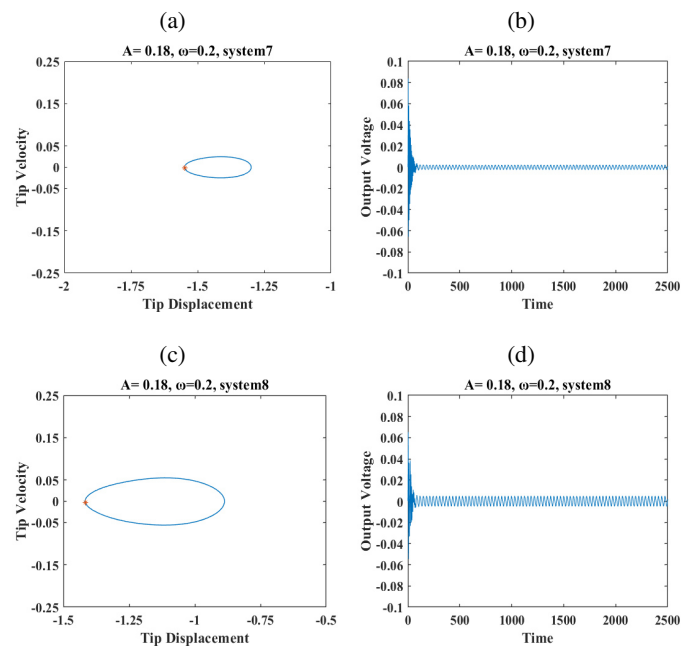

Fig. 17. Phase diagram (blue lines in left column), Poincaré map (red points in left column) and voltage response (right column) at $\omega = 0.2$ and $A = 0.18$ for (a) and (b) system 7; (c) and (d) system 8; (e) and (f) system 9

coexisting oscillation, generating higher output power. The fact that the potential well of system 9 is lower than that of system 0 contributes to larger displacement orbit of system 9. The bifurcation diagram of system 9 is shown in Fig. 16(b). Within the excitation amplitude range, the motion change laws of system 9 are as follows: single-period motion – multiple period motion.

4.3.2. Effect of excitation frequency on harvesting performance

Excitation amplitude $A = 0.04$ and excitation frequency ranging from 0.1 to 1.2 is adopted to examine the dynamic response of group 3 systems.
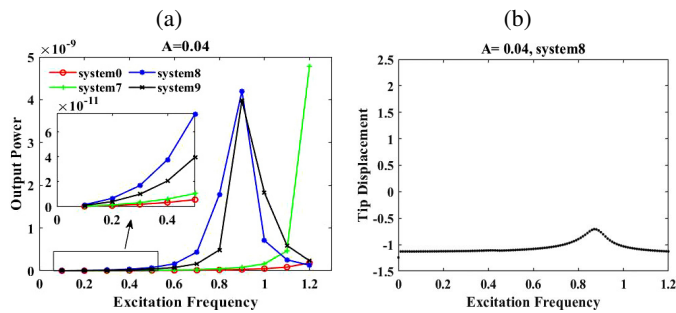

Fig. 18. Output power of group 3 systems at $A = 0.04$ for (a) andbifurcation diagram of system 8 at $A = 0.04$ for (b)

The output powers of systems 7 to 9 are shown as Fig. 18(a). It is obvious that systems 8 and 9 reach higher harvesting performance near $\omega = 0.9$, in contrast to system 0. System 7 has better output performance in extremely higher excitation frequency range [1, 1.2]. For excitation frequency $\omega = 0.9$, the phase diagram and Poincaré map of systems 7 to 9 are shown in Fig. 19. It can be seen from those that both systems 8 and 9
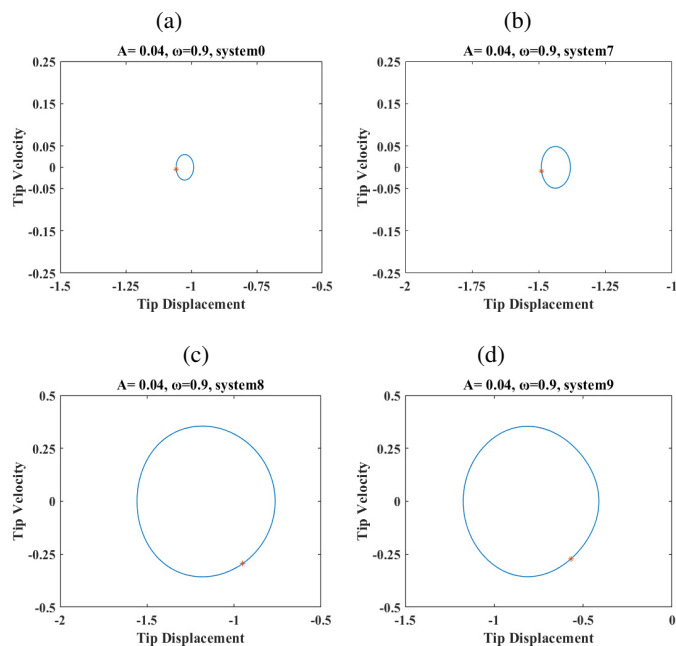

Fig. 19. Phase diagram (blue lines) and Poincaré map (red points) at $\omega = 0.9$ and $A = 0.04$ for (a) system 0; (b) system 7; (c) system 8; (d) system 9

generate highest output power at excitation frequency $\omega = 0.9$, but the bandwidth of system 8 is broader than that of system 9. However, system 7 can produce higher output power than systems 8 and 9 only at high excitation frequency. The bifurcation diagram of system 8 is shown in Fig. 18(b). According to the bifurcation diagram, system 8 enters intra-well orbits near excitation frequency amounting to 0.9 and generates the highest output performance, which is consistent with the status in Fig. 18(a).

5. DISCUSSION

To investigate the effect of excitation amplitude, Fig. 6(a), 11(a), and 16(a) are compared. It is found that horizontal spacing s affects the output power and most of systems present higher output power than TBEH with lower excitation level, $A = [0.02, 0.1]$. Also, if $s = 0$, the output power for excitation level $A = [0.02, 0.1]$ is lower than for other horizontal spacing values. It seems that the systems with vertical spacing of 13 mm and 15 mm, respectively, show more significant performance within low excitation levels. Table 3 shows the output power of the systems with different s and c when $A = 0.06$. By comparing these figures, it is noted that systems 5 and 6 achieve higher output power than other systems when the excitation amplitude A is as low as 0.06.

Table 3
Output power with different s and c when $A = 0.06$ ($\omega = 0.2$)

s	$c = 11$ mm	$c = 13$ mm	$c = 15$ mm
$s = -2$ mm	2.64×10^{-11}	1.02×10^{-11}	1.58×10^{-11}
$s = 0$ mm	1.68×10^{-12}	5.78×10^{-09}	1.57×10^{-09}
$s = 2$ mm	3.15×10^{-12}	1.50×10^{-11}	9.26×10^{-12}

As for the effect of excitation frequency, it is found from Fig. 8(a), 13(a) and 18(a) that as horizontal spacing s moves from –2 mm to 2 mm, the frequencies of maximum output power for the systems shift from the right of TBEH to the left as well. This means the systems can improve their harvesting efficiency within lower frequencies. It is also found that the systems with vertical spacing of 13 mm and 15 mm, respectively, are helpful for higher harvesting efficiency within low excitation frequencies. Furthermore, the systems with vertical spacing of 13 mm and 15 mm have larger bandwidth than the systems with other vertical displacements. Table 4 shows the output power of the systems with different s and c when $\omega = 0.3$. By comparing these figures, it is noted that systems 1, 5 and 6 would be better for low excitation frequencies.

The comparison of the bandwidth and output power of different systems is listed in Table 5 when excitation amplitude $A = 0.04$, for example. The bandwidth is regarded as effective when the output power is higher than 1×10^{-09}. From Table 5 it appears that system 6 reaches the maximum bandwidth with the range of [0.169, 0.576], and system 1 gets the bandwidth ranging from 0.613 to 0.865. However, the bandwidths of system 0 or the TBEH are much smaller than those of other sys-

Investigation of the influence of additional magnets positions on four-magnet bi-stable piezoelectric energy harvester

Table 4
Output power with different s and c when $\omega = 0.3$ ($A = 0.04$)

s	$c = 11$ mm	$c = 13$ mm	$c = 15$ mm
$s = -2$ mm	3.17×10^{-11}	1.12×10^{-11}	1.75×10^{-11}
$s = 0$ mm	1.71×10^{-12}	2.95×10^{-11}	1.47×10^{-09}
$s = 2$ mm	3.26×10^{-12}	1.69×10^{-11}	9.98×10^{-12}

Table 5
Bandwidth of operation frequency (BOF) and maximum power (MP) for FBEHs at $A = 0.04$

System No.	BOF	The range of BOF	MP
0	0	–	1.82×10^{-10}
1	0.252	[0.613, 0.865]	3.14×10^{-09}
2	0.255	[0.825, 1.08]	2.97×10^{-09}
3	0.225	[0.765, 0.99]	3.65×10^{-09}
4	0	–	1.43×10^{-10}
5	0.208	[0.66, 0.868]	1.52×10^{-09}
6	0.407	[0.169, 0.576]	2.75×10^{-09}
7	0.09	[1.11, 1.2]	4.78×10^{-09}
8	0.25	[0.742, 0.992]	4.20×10^{-09}
9	0.256	[0.814, 1.07]	3.98×10^{-09}

tems. Moreover, system 0 gets nearly the lowest output power in these systems. Hence, it is known that FBEH systems are available for improving the output power and the bandwidth of BEH, especially with low excitation amplitudes.

6. CONCLUSIONS

In this paper, the proposed FBEH introduced two additional magnets C and D on TBEH, leading to realizing potential energy performance improvement over TBEH. Taking the horizontal and vertical gap of magnets as variable parameters, 9 FBEH systems with different potential wells were established. Through numerical simulations, their output performances were investigated, and then the conclusions can be drawn as follows:

- FBEH presents the characteristics that are bi-stable or sometimes accompanied by tri-stable behaviors, which is beneficial for improving output performance at low excitation frequencies by adjusting horizontal and vertical gaps between magnets C and D.
- FBEH generated electric energy that is relatively high when it enters the high-energy orbit. Chaotic motion is more likely to be exhibited under lower excitation amplitudes, which improves the output performance of FBEH. Through choosing the appropriate magnetic distance parameters, the FBEH can jump into chaotic motion state over a wider frequency range, and can effectively improve its output power even under low excitation levels and frequencies.
- FBEH can shift its effective bandwidth from right to left. This is more helpful for harvesting energy under low-

frequency excitation. Furthermore, FBEH extends the harvesting bandwidth and improves energy harvesting efficiency of the harvester as a result.

REFERENCES

[1] F.K. Shaikh and S. Zeadally, "Energy harvesting in wireless sensor networks: A comprehensive review", *Renew. Sustain. Energy Rev.*, vol. 55, pp. 1041–1054, 2016, doi: 10.1016/j.rser.2015.11.010.

[2] M.T. Todaro *et al.*, "Piezoelectric MEMS vibrational energy harvesters: Advances and outlook", *Microelectron. Eng.*, vol. 183–184, pp. 23–36, 2017, doi: 10.1016/j.mee.2017.10.005.

[3] F. Ali, W. Raza, X. Li, H. Gul, and K.H. Kim, "Piezoelectric energy harvesters for biomedical applications", *Nano Energy*, vol. 57, pp. 879–902, 2019, doi: 10.1016/j.nanoen.2019.01.012.

[4] M.R. Sarker, S. Julai, M.F.M. Sabri, S.M. Said, M.M. Islam, and M. Tahir, "Review of piezoelectric energy harvesting system and application of optimization techniques to enhance the performance of the harvesting system", *Sensors Actuators, A Phys.*, vol. 300, p. 111634, 2019, doi: 10.1016/j.sna.2019.111634.

[5] N. Tran, M. H. Ghayesh, and M. Arjomandi, "Ambient vibration energy harvesters: A review on nonlinear techniques for performance enhancement", *Int. J. Eng. Sci.*, vol. 127, pp. 162–185, 2018, doi: 10.1016/j.ijengsci.2018.02.003.

[6] C. Wei and X. Jing, "A comprehensive review on vibration energy harvesting: Modelling and realization", *Renew. Sustain. Energy Rev.*, vol. 74, pp. 1–18, 2017, doi: 10.1016/j.rser.2017.01.073.

[7] T. Yildirim, M.H. Ghayesh, W. Li, and G. Alici, "A review on performance enhancement techniques for ambient vibration energy harvesters", *Renew. Sustain. Energy Rev.*, vol. 71, pp. 435–449, 2017, doi: 10.1016/j.rser.2016.12.073.

[8] H. Liu, J. Zhong, C. Lee, S.W. Lee, and L. Lin, "A comprehensive review on piezoelectric energy harvesting technology: Materials, mechanisms, and applications", *Appl. Phys. Rev.*, vol. 5, no. 4, 2018, doi: 10.1063/1.5074184.

[9] A. Erturk and D.J. Inman, "A distributed parameter electromechanical model for cantilevered piezoelectric energy harvesters", *J. Vib. Acoust. Trans. ASME*, vol. 130, no. 4, pp. 1–15, 2008, doi: 10.1115/1.2890402.

[10] Y. Yang and L. Tang, "Equivalent circuit modeling of piezoelectric energy harvesters", *J. Intell. Mater. Syst. Struct.*, vol. 20, no. 18, pp. 2223–2235, 2009, doi: 10.1177/1045389X09351757.

[11] L. Yu, L. Tang, and T. Yang, "Piezoelectric passive self-tuning energy harvester based on a beam-slider structure", *J. Sound Vib.*, vol. 489, p. 115689, 2020, doi: 10.1016/j.jsv.2020.115689.

[12] M. Sayed, A.A. Mousa, and I. Mustafa, "Stability and bifurcation analysis of a buckled beam via active control", *Appl. Math. Model.*, vol. 82, pp. 649–665, 2020, doi: 10.1016/j.apm.2020.01.074.

[13] S. Zhou, J. Cao, and J. Lin, "Theoretical analysis and experimental verification for improving energy harvesting performance of nonlinear monostable energy harvesters", *Nonlinear Dyn.*, vol. 86, no. 3, pp. 1599–1611, 2016, doi: 10.1007/s11071-016-2979-7.

[14] H. T. Nguyen, D. Genov, and H. Bardaweel, "Mono-stable and bi-stable magnetic spring based vibration energy harvesting systems subject to harmonic excitation: Dynamic modeling and experimental verification", *Mech. Syst. Signal Process.*, vol. 134, p. 106361, 2019, doi: 10.1016/j.ymssp.2019.106361.

[15] T. Huguet, A. Badel, O. Druet, and M. Lallart, "Drastic bandwidth enhancement of bistable energy harvesters: Study of subharmonic behaviors and their stability robustness", *Appl. Energy*, vol. 226, pp. 607–617, 2018, doi: 10.1016/j.apenergy.2018.06.011.

[16] H. Wang and L. Tang, "Modeling and experiment of bistable two-degree-of-freedom energy harvester with magnetic coupling", *Mech. Syst. Signal Process.*, vol. 86, pp. 29–39, 2017, doi: 10.1016/j.ymssp.2016.10.001.

[17] Y. Zhang, Y. Leng, S. Fan, "The Accurate Analysis of Magnetic Force of Bi-stable Piezoelectric Cantilever Energy Harvester", presented at the *ASME International Design Engineering Technical Conferences/Computers and Information in Engineering Conference*, Cleveland, Ohio, USA, 2017, doi: 10.1115/DETC2017-67168.

[18] T. Tan, Z. Yan, K. Ma, F. Liu, L. Zhao, and W. Zhang, "Nonlinear characterization and performance optimization for broadband bistable energy harvester", *Acta Mech. Sin. Xuebao*, vol. 36, no. 3, pp. 578–591, 2020, doi: 10.1007/s10409-020-00946-3.

[19] K. Wang, X. Dai, X. Xiang, G. Ding, and X. Zhao, "Optimal potential well for maximizing performance of bi-stable energy harvester", *Appl. Phys. Lett.*, vol. 115, no. 14, 2019, doi: 10.1063/1.5095693.

[20] V. Shah, R. Kumar, M. Talha, and J. Twiefel, "Numerical and experimental study of bistable piezoelectric energy harvester", *Integr. Ferroelectr.*, vol. 192, no. 1, pp. 38–56, 2018, doi: 10.1080/10584587.2018.1521669.

[21] T. Yang and Q. Cao, "Dynamics and high-efficiency of a novel multi-stable energy harvesting system", *Chaos Solitons Fractals*, vol. 131, p. 109516, 2020, doi: 10.1016/j.chaos.2019.109516

[22] Z. Zhou, W. Qin, and P. Zhu, "Improve efficiency of harvesting random energy by snap-through in a quad-stable harvester", *Sens. Actuators, A*, vol. 243, pp. 151–158, 2016, doi: 10.1016/j.sna.2016.03.024.

[23] M. Panyam and M.F. Daqaq, "Characterizing the effective bandwidth of tri-stable energy harvesters", *J. Sound Vib.*, vol. 386, pp. 336–358, 2017, doi: 10.1016/j.jsv.2016.09.022.

[24] Y. Leng, D. Tan, J. Liu, Y. Zhang, and S. Fan, "Magnetic force analysis and performance of a tri-stable piezoelectric energy harvester under random excitation", *J. Sound Vib.*, vol. 406, pp. 146–160, 2017, doi: 10.1016/j.jsv.2017.06.020.

[25] M. Lallart, S. Zhou, Z. Yang, L. Yan, K. Li, and Y. Chen, "Coupling mechanical and electrical nonlinearities: The effect of synchronized discharging on tristable energy harvesters", *Appl. Energy*, vol. 266, no. January, p. 114516, 2020, doi: 10.1016/j.apenergy.2020.114516.

[26] J. Wang and Z. Wang, "A double bi-stable energy harvester for enhanced ability of bi-stable energy harvesting from random vibration", *J. Appl. Sci. Eng.*, vol. 20, no. 3, pp. 387–392, 2017, doi: 10.6180/jase.2017.20.3.13.

[27] G. Wang, W. Liao, B. Yang, X. Wang, W. Xu, and X. Li, "Dynamic and energetic characteristics of a bistable piezoelectric vibration energy harvester with an elastic magnifier", *Mech. Syst. Signal Process.*, vol. 105, pp. 427–446, 2018, doi: 10.1016/j.ymssp.2017.12.025.

[28] Z. Zhou, W. Qin, W. Du, P. Zhu, and Q. Liu, "Improving energy harvesting from random excitation by nonlinear flexible bistable energy harvester with a variable potential energy function", *Mech. Syst. Signal Process.*, vol. 115, pp. 162–172, 2019, doi: 10.1016/j.ymssp.2018.06.003.

[29] X. Li *et al.*, "Broadband spring-connected bi-stable piezoelectric vibration energy harvester with variable potential barrier", *Results Phys.*, vol. 18, no. May, p. 103173, 2020, doi: 10.1016/j.rinp.2020.103173.

[30] S. Zhou, J. Cao, D.J. Inman, J. Lin, S. Liu, and Z. Wang, "Broadband tristable energy harvester: Modeling and experiment verification", *Appl. Energy*, vol. 133, pp. 33–39, 2014, doi: 10.1016/j.apenergy.2014.07.077.

[31] Z. Zhou, W. Qin, Y. Yang, and P. Zhu, "Improving efficiency of energy harvesting by a novel penta-stable configuration", *Sensors Actuators A.*, vol. 265, pp. 297–305, 2017, doi: 10.1016/j.sna.2017.08.039.

[32] D. Huang, S. Zhou, and G. Litak, "Theoretical analysis of multistable energy harvesters with high-order stiffness terms", *Commun. Nonlinear Sci. Numer. Simul.*, vol. 69, pp. 270–286, 2019, doi: 10.1016/j.cnsns.2018.09.025.

[33] C. Lan and W. Qin, "Enhancing ability of harvesting energy from random vibration by decreasing the potential barrier of bistable harvester", *Mech. Syst. Signal Process.*, vol. 85, pp. 71–81, 2017, doi: 10.1016/j.ymssp.2016.07.047.

[34] M. Ostrowski, B. Błachowski, M. Bocheński, D. Piernikarski, P. Filipek, and W. Janicki, "Design of nonlinear electromagnetic energy harvester equipped with mechanical amplifier and spring bumpers", *Bull. Polish Acad. Sci. Tech. Sci.*, vol. 68, no. 6, pp. 1373–1383, 2020, doi: 10.24425/bpasts.2020.135384.

[35] D. Tan, Y.G. Leng, and Y.J. Gao, "Magnetic force of piezoelectric cantilever energy harvesters with external magnetic field", *Eur. Phys. J. Spec. Top.*, vol. 224, no. 14–15, pp. 2839–2853, 2015, doi: 10.1140/epjst/e2015-02592-6.

12

Bull. Pol. Acad. Sci. Tech. Sci., vol. 70, no. 1, p. e140151, 2022